Micelle size and orientational order across the nematic-isotropic transition: A field-dependent nuclear-spin-relaxation study

István Furó and Bertil Halle

Condensed Matter Magnetic Resonance Group, Chemical Center, Lund University, P.O. Box 124, S-22100 Lund, Sweden

(Received 17 June 1994)

Magnetic field-dependent counterion ^{23}Na spin relaxation and quadrupole splitting measurements are reported from the discotic nematic (N_D) and isotropic phases of the system sodium dodecylsulphate–decanol–water. Carefully designed relaxation experiments were used to determine the individual field-dependent motional spectral densities. A quantitative analysis of the splitting and spectral density data allowed a simultaneous determination of the nematic order parameter S and the axial ratio of the disklike micelles as functions of temperature throughout the extension of the N_D phase and into the isotropic phase. The axial ratio varies only weakly with temperature in the N_D phase, from 6 at 10 °C below the nematic-isotropic transition temperature T_{NI} to 4 just below T_{NI}, but then increases to 8 in the isotropic phase just above T_{NI}. This behavior is contrary to the existing theoretical predictions. The nematic order parameter decreases from 0.9 at 10 °C below T_{NI} to 0.4 just below T_{NI}. While the latter value is close to that predicted by Maier-Saupe theory, the temperature dependence of S is much stronger than that predicted theoretically.

PACS number(s): 61.30.Eb, 61.30.Gd, 64.70.Md, 76.60.Es

I. INTRODUCTION

An orientationally ordered but positionally disordered bulk fluid is referred to as a nematic phase. Such nematic phases can be formed in a variety of low-molecular weight or polymer liquids (thermotropic molecular or polymer nematics) as well as in complex (organized, multicomponent) fluids consisting of amphiphilic aggregates or colloidal particles in a (usually aqueous) solvent (lyotropic amphiphilic or colloidal nematics). Whereas the classical molecular nematic phase and its transition to an isotropic phase have been studied extensively [1] and are reasonably well understood, relatively little is known about amphiphilic nematics [2–5].

Although similar at a phenomenological level, molecular and amphiphilic nematics differ fundamentally at the molecular level; the orientationally ordered entities being molecules and molecular aggregates, respectively. One of the major experimental challenges posed by amphiphilic nematics is to simultaneously determine the size of the micellar aggregates, or their axial ratio, ρ, and their orientational order parameter $S = \langle P_2(\cos\theta) \rangle$, with θ the angle between the symmetry axes of the micelle and the phase.

Quadrupole splittings in NMR spectra have been used extensively to study amphiphilic nematics [2–4]. While the quadrupole splitting contains information about both ρ and S, this information is not separable. A reduction of the splitting with increasing temperature can thus be due to a smaller order parameter, a smaller micelle size, or a combination thereof. As recently demonstrated, however, the separation problem can be overcome [6]. The spin relaxation of nuclei residing in counterions or amphiphilic molecules reflect molecular diffusion over the curved surface of orientationally disordered micelles and thus de-

pends on both ρ and S [7]. By combining splitting and relaxation data from the same quadrupolar nucleus, it is thus possible to separately determine ρ and S.

We report here a study of a sample in the system sodium dodecylsulphate (SDS)–decanol–water, which transforms from a discotic nematic (N_D) phase to an isotropic micellar solution at 29.3 °C. Using nuclear-spin-relaxation methods, we have previously studied the nematic (N_C and N_D) [6], hexagonal (H_α) [8], and lamellar (L_α) [9] phases of the same system at compositions not far from the present one. In the previous study of the nematic phases [6], a detailed analysis of the relaxation data was possible only by invoking reference parameters determined in the nearby H_α phase. While these parameters (residual quadrupole coupling constant, surface diffusion coefficient, local reorientational dynamics) should be closely similar in the H_α and N_C phases, which have similar interface curvature, the transferability of the H_α parameters to the N_D phase (with a distinctly smaller average mean curvature) is more uncertain. In the present study, we circumvented this problem by performing spin relaxation measurements, on the counterion ^{23}Na nuclei, over a range of magnetic fields spanning the major part of the relaxation dispersion of the crucial surface-diffusion contribution.

At the composition of the previous study [6], the N_D phase transforms into an N_C phase at 28.8 °C. In contrast, the present sample, which has the same SDS:decanol mole ratio but a slightly lower micelle volume fraction, transforms into an isotropic phase (I) at 29.3 °C. Since the spin relaxation method is more sensitive to micelle size (ρ) for disklike (or oblate spheroidal) micelles than for rodlike (or prolate spheroidal) micelles, the present sample is well suited for investigating changes in micelle size at the nematic-to-isotropic $(N\text{-}I)$ transi-

tion. Furthermore, the variation of the order parameter S with temperature on approaching the N-I transition is of fundamental interest, as it reflects the anisotropic intermicellar interactions that are responsible for the long-range orientational order of the nematic phase.

II. EXPERIMENT

A. Materials and sample preparation

Sodium dodecylsulphate (specially pure) and decanol (n-decanol, specially pure) from BDH Chemicals were used as supplied. ^{17}O enriched deuterium oxide from Ventron was mixed with normal millipore water yielding ^{17}O and ^2H enrichments of 3.7% and 17.0%, respectively. The N_D sample, containing 21.02 wt % SDS, 4.61 wt % decanol, and 74.37 wt % water, was prepared as previously described [6]. As may be seen form the partial phase diagram in Fig. 1, this sample composition slightly extends the previously reported [6,9] range of the N_D phase [P-O. Quist (unpublished)]. The molar composition and micelle volume fraction of the present sample, as well as the previously studied samples of the same system, are given in Table I.

The nematic phase was stable from ca. 16 °C (where SDS precipitates) to T_{NI} = 29.3±0.1 °C. A narrow two-phase region, with the N_D phase in equilibrium with the isotropic micellar solution phase, occurs between T_{NI} and T_{IN} = 29.55±0.1 °C. The N_D-I transition occurs only in a narrow concentration range; a slight increase of the decanol/SDS ratio changes the transition to N_D-L_α. At ca. 33 °C, the isotropic phase transformed into another

anisotropic phase (probably L_α), exhibiting a broad, anisotropic NMR spectrum.

After preparation, the sample was kept for 11 weeks at 25 °C, during which time the aforementioned transition temperatures changed by ca. 0.2 °C. During the measurement period of ca. five weeks no shifts of transition temperatures were detected. (The sample was kept frozen between experiments separated by more than two days.)

B. Spectrometer and magnet characteristics

The NMR experiments were performed on a Bruker MSL-100 spectrometer, equipped with both a superconducting magnet and an electromagnet. During the measurements, the sample was kept in a flame-sealed 10 mm o.d. NMR tube filled to 28 mm height. The experiments at 2.35 T were carried out on the superconducting magnet with a 10 mm saddle-coil probe. The spatial inhomogeneity of the radio frequency (rf) field was less than ±10% within the sample volume, while the inhomogeneity of the static magnetic field was a few Hz. For the experiments in the magnetic field range 0.2–2.0 T, we used an electromagnet (Drusch EAR-35N), equipped with a field-variable NMR lock (RMN2-TAO2) and a flux stabilizer from the same company. The solenoid NMR probes (type Bruker Z-22V) had less than ±3% RF inhomogeneity within the sample volume.

Since field dispersion measurements on an electromagnet are nonstandard and since optimization of accuracy and precision was important in the present study, we record some relevant system characteristics. The instability of the magnetic field includes a long-time drift not fully compensated by the NMR lock, mainly due to the spatial separation of the lock and the NMR coils. This drift becomes negligible 2–3 h after switching on the system or ca. 1 h after a major field change. The short-term noise, on a time scale of 1–10 s, was minimized by adjusting the relative gains of the NMR lock and the flux stabilizer. The field stability (peak-to-peak) achieved was ±0.15 μT at the extremes of the 0.2–2.0 T range and
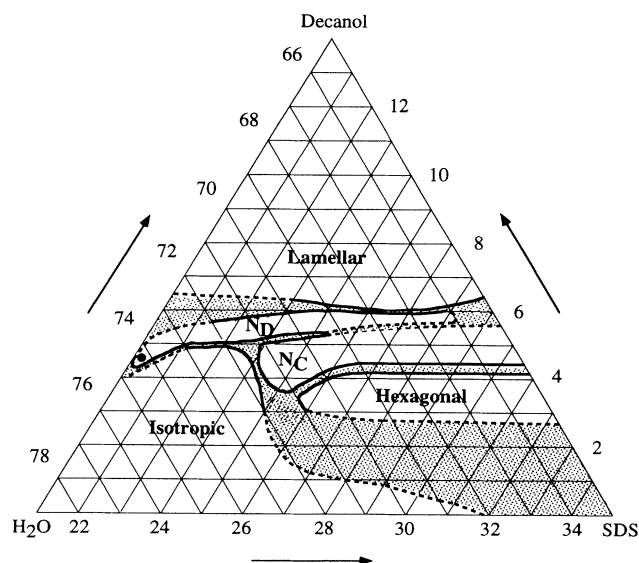

Decanol

FIG. 1. Partial phase diagram (wt %) for the system SDS-decanol-water (90% H_2O:10% D_2O) at 25 °C, showing the extension of the one-phase regions of the isotropic micellar solution phase and the lamellar, hexagonal, and nematic (N_C,N_D) liquid-crystalline phases. (The dashed boundaries have not been precisely located.) The dot in the N_D phase corresponds to the composition of the sample investigated here.

TABLE I. Molar compositions, micelle volume fractions, and residual ^{23}Na quadrupole coupling constants in the lamellar, hexagonal, and nematic phases of the system SDS-decanol-water investigated by ^{23}Na NMR.

Phase Examined T range (°C)	H_α 23–35	N_C 15–28	L_α[a] 25	N_D 15–29	N_D 19–29
$n_{dec}/(n_{SDS}+n_{dec})$[b]	0.196	0.247	0.318	0.287	0.285
$n_W/(n_{SDS}+n_{dec})$[b]	34.6	34.5	26.0	32.2	39.2
ϕ[c]	0.272	0.266	0.326	0.280	0.242
$\bar{\chi}$ (kHz)[d]	79	79[e]	104[f]	98[g]	108
References	[8]	[6]	[9]	[6]	this work

[a]Disrupted bilayers, probably ribbonlike aggregates.
[b]n = number of moles.
[c]Micelle volume fraction.
[d] ^{23}Na residual quadrupole coupling constant at 25 °C.
[e]Taken to be the same as in the H_α phase.
[f]Assuming elliptic ribbon microstructure.
[g]Taken to be 25% larger than in the H_α phase to obtain agreement between the reduced ^2H and ^{23}Na splittings.

$\le \pm 0.11$ μT in the range 0.3–1.5 T. Besides these instabilities, external transients may cause large (in the order of 10–100 μT) field jumps. By extensive shielding and grounding, we could limit the significant effects of such transients to less than 0.01% of the measurement time. The system remained susceptible to disturbances from a few strong external radiobands, which, however, were narrow and thus easily avoided.

To reduce the spectral noise, particularly important at the lowest frequencies, we used double- and triple-shielded coaxial cables. The orthonormality of the four rf channels used in phase cycling as well as the phase and amplitude balance of the receiver were carefully adjusted. The practical low-frequency limit ca. 2.3 MHz is set by the drastic fall in preamplifier gain below this frequency. The achievable signal-to-noise ratios are demonstrated in Fig. 2. Ringing after the rf pulses, most persistent at 5–7 MHz, did not exceed 200 μs. The inhomogeneity of the static field was about 1–1.2 μT at the higher fields (≥ 0.8 T) and about 0.3–0.4 μT at the lower fields (≤ 0.5 T). The length of the 180° rf pulse was 10–12 μs. Below 5 MHz the rf pulses showed significant "phase glitches," the effect of which was suppressed by phase cycling and by the data evaluation procedure described below.

The temperature was controlled by a Stelar VTC87 regulator with a high airflow (1.5 m^3 h^{-1} on the superconducting magnet and ≤ 1 m^3 h^{-1} on the electromagnet). The airflow on the electromagnet system was reduced to avoid sample vibration. While the temperature stability was similar ($\pm$ca. 0.03–0.04 °C) for the two different setups, the temperature gradient was smaller for the superconducting system (≤ 0.04 °C) than for the electromagnetic system (ca. 0.06 °C). To obtain a stable and homogeneous temperature, it was found essential to center the sample tube properly and to use probe head dewards that minimize airflow turbulence.

C. Spin relaxation experiments

The ^{23}Na spin relaxation is purely quadrupolar and the response of the $I = \frac{3}{2}$ spin system to the pulse sequences used here has been described elsewhere [8,11]. The longitudinal spin relaxation behavior is governed by the two lab-frame spectral densities $J_1^L(\omega_0)$ and $J_2^L(2\omega_0)$, which were determined in the magnetic field range 0.20–2.35 T, corresponding to Larmor frequencies $\omega_0/(2\pi) = 2.30$ –26.49 MHz, using two or three independent relaxation experiments. At fields above 0.5 T, the relaxation experiments were (i) inversion recovery with 90° detection pulse, (ii) inversion recovery with short (ca. 35°) detection pulse, and (iii) the quadrupole polarization decay experiment, using the Jeener-Broekaert pulse sequence [10,11]. The coupled evolution of the dipolar and octupolar polarizations generally yields a biexponential inversion recovery, while the quadrupole polarization decay is single exponential. The relaxation functions for the different spectral lines in the inversion recovery experiments are collected in Table II. Monte Carlo simulations show that this combination of relaxation experiments minimizes the systematic error in the determination of the individual spectral densities $J_1^L(\omega_0)$ and $J_2^L(2\omega_0)$ [I. Furó, (unpub-

lished)].

In all relaxation experiments the acquisition delay after the last rf pulse was set equal to the inverse quadrupole splitting (or half of this value, yielding inverted satellites) in order to obtain pure absorption line shapes without first-order phase corrections. The phase of the detection pulses was cycled to suppress the effects of nonideal inversion pulses [8]. A typical experiment comprised 30 delay times, more closely spaced near the average decay time [12]. Line intensities were obtained by integrating the absorption lines, typically over a range of ± 3 linewidths. The errors in these intensities were assessed by collecting spectral noise over a corresponding frequency range. These error estimates account for the random spectral noise, but not for the instability of magnetic field, rf phase and any rf component of the spectrometer. In a few cases (especially at the highest fields with small spectral noise), whereas the fitting results indicated that such instabilities were significant, we increased the noise input to satisfy our goodness-of-fit criterion.

Rather than extracting relaxation rates from each experiment, we determined the two spectral densities directly from a simultaneous fit to all five relaxation decays. (The intensities of the two satellites were added in the inversion recovery experiments and subtracted in the quadrupole polarization decay experiment.) One such fit, involving eight free parameters, is shown in Fig. 3. In Table III, we present the spectral densities at the investigated temperatures (in the nematic phase) and magnetic fields.

By including the detection pulse angle among the parameters, systematic errors due to rf inhomogeneity, inaccurate pulse length settings, and "phase glitches" were avoided. The initial and long-time intensities in the inversion recovery experiment were treated as independent parameters, thus allowing for rf inhomogeneity. The relative amplitude of the central and satellite lines was also adjustable, allowing for uncertainties in the integration ranges. To account for a possible deviation form nonselective rf pulses. [I. Furó (unpublished)], correction factors multiplying some line intensities were introduced in the fit to the 19 °C data, with the largest quadrupole splitting. These corrections were always close to 1 and their inclusion changed the spectral densities by less than 1%. The internal consistency of the relaxation data was tested at high fields by fitting all different combinations of 2, 3, or 4 decays; the results coincided within the error limits given in Table III, thus demonstrating the robustness of the applied procedure.

At the lowest fields (≤ 0.5 T), the satellite lines were too noisy to be evaluated. The two spectral densities were, therefore, determined from the decay of the central line in the two inversion recovery experiments, which, at high fields, were shown to yield the same results as a fit to all five decays.

Although the individual spectral densities from $I = \frac{3}{2}$ nuclei in isotropic solutions can be determined by various relaxation experiments [13–15], this was not possible here due to the relatively large inhomogeneity of the static magnetic field and the closeness of the spectral densities $J(\omega_0)$ and $J(2\omega_0)$. Instead, the inversion recovery de-

TABLE II. The dependence of the decay functions of the various lines on the length of the detection pulse θ in the inversion recovery experiment [11].

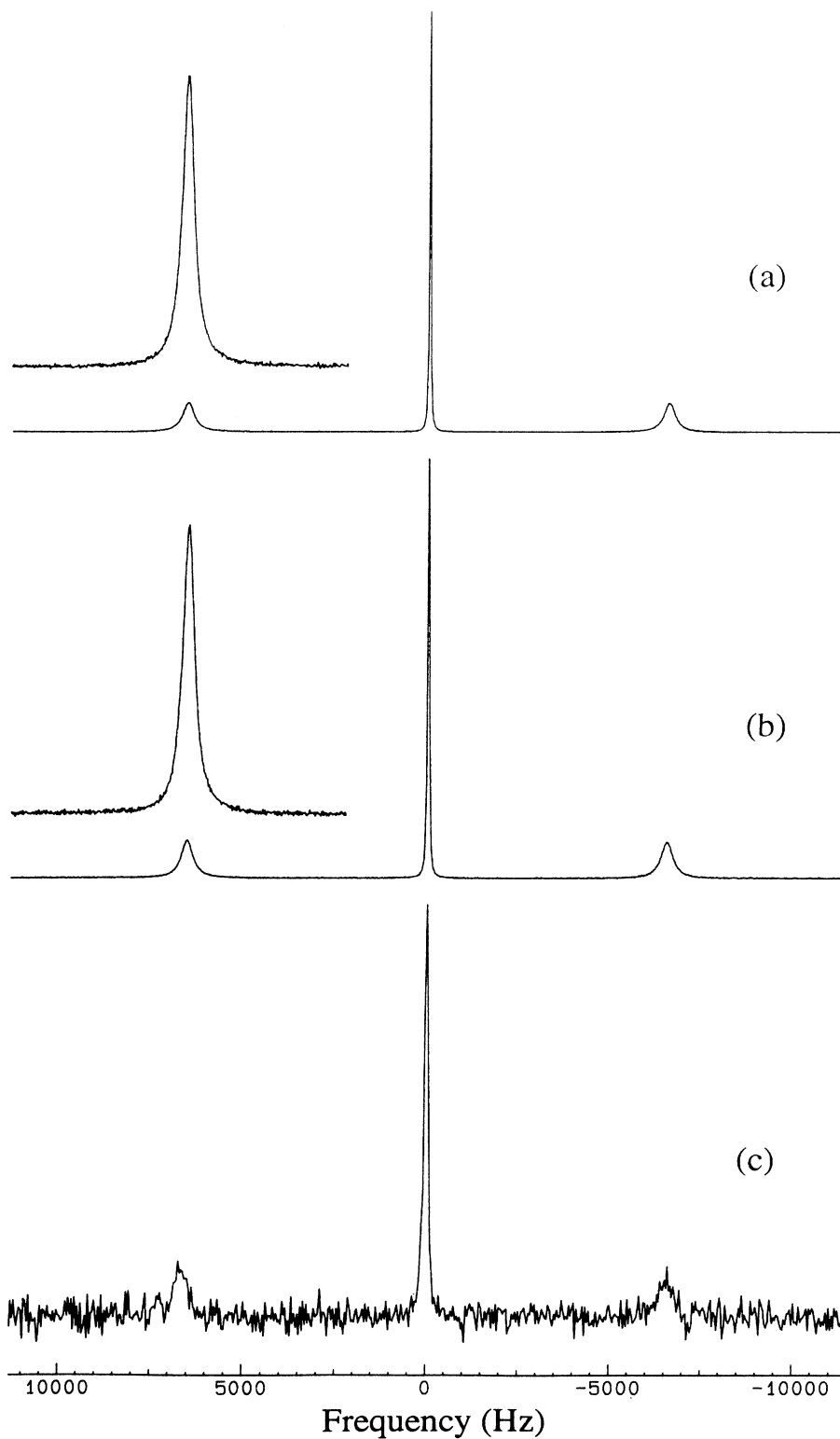| Line	Spectral intensity
Satellite	$\frac{3}{10}\sin\theta[1-2\cos^2\theta\exp(-\alpha j_1\tau)-2\sin^2\theta\exp(-\alpha j_2\tau)]$
Central	$\frac{4}{10}\sin\theta[1-(1-3\cos^2\theta)\exp(-\alpha j_1\tau)-(1+3\cos^2\theta)\exp(-\alpha j_2\tau)]$

(a)

(b)

(c)

FIG. 2. ^{23}Na spectra obtained in the inversion recovery experiments at the longest delay times. 1024 transients were collected at 2.35 and 2.0 T [(a) and (b), respectively] and 8000 transients at 0.204 T (c). The signal-to-noise ratio was roughly a factor of 2 higher at 2.35 T than at 2.0 T (cf. magnified satellite peaks).

Frequency (Hz)

TABLE III. Magnetic field dependence of lab-frame spectral densities of ^{23}Na in the N_D phase.

	$J_1^L(\omega_0)(s^{-1})$				$J_2^L(2\omega_0)(s^{-1})$			
$B_0(T)^a$	19°C	25°C^b	28°C	29°C	19°C	25°C^b	28°C	29°C
0.204	180±10	180±9	184±11	178±7	159±5	144±4	134±6	139±4
0.50	115.0±1.0	112.8±1.0	110.8±0.9	112.3±0.6	105.0±0.5	94.6±0.4	89.2±0.5	86.1±0.3
1.00	81.1±0.5	78.9±0.5	77.9±0.7	77.1±0.5	78.4±0.3	68.9±0.2	64.0±0.3	61.7±0.2
2.00	63.4±0.3	58.2±0.2	56.8±0.2	56.5±0.2	62.0±0.2	53.0±0.2	48.8±0.2	46.8±0.2
2.35	60.1±0.2	54.8±0.2	53.0±0.2	53.1±0.3	58.9±0.2	50.3±0.2	46.3±0.2	44.4±0.2

^{a}For ^{23}Na, the relation between the Larmor frequency ω_0 and the magnetic field strength B_0 is $\omega_0(\text{rad s}^{-1}) = 7.08 \times 10^7 B_0(T)$.
^{b}Three additional magnetic fields were included at 25°C—see Fig. 7.

cay was fitted to a single exponential and the effective relaxation rate R_1^* was used for the subsequent analysis.

III. QUADRUPOLE SPLITTING

The quadrupole splitting, v_Q, of a spin $I = \frac{3}{2}$ nucleus like ^{23}Na in a diamagnetically negative phase (with the symmetry axis of the phase perpendicular to the magnetic field) is given by

$$v_Q = \frac{1}{4} |A(\rho)S\bar{\chi}| . \tag{3.1}$$

The shape function $A(\rho) = \langle P_2(\cos\theta_{AN}) \rangle$ is the second-rank orientational order parameter associated with the angle θ_{AN} between the symmetry axis of the (uniaxial) micellar aggregate and the local surface normal, and the average is taken over the surface of the micelle. If the spatial distribution of Na$^+$ counterions, projected on this surface, is laterally uniform, then A is a unique function of the micellar axial ratio ρ, readily calculated for any unixial shape.

As seen from Fig. 4, the counterion ^{23}Na splitting varies strongly with temperature as the N_D-I transition is approached. This contrasts with the much weaker tem-

perature dependence near the N_D-N_C transition. According to (3.1), the observed variation of v_Q can be due to a temperature dependence in the axial ratio ρ, the nematic order parameter S, the residual quadrupole coupling constant (QCC) $\bar{\chi}$, or some combination thereof. From a previous study [8] of the nearby H_α phase, where $A \approx -\frac{1}{2}$ and $S \approx 1$, we know that $\bar{\chi}$ varies little with temperature and, hence, can account for only a minor fraction of the temperature dependence of v_Q seen in Fig. 4. This conclusion can be checked by measuring the ^{2}H and ^{17}O quadrupole splittings of the water nuclei in the N_D sample. Since the residual QCC has different origins for counterions [16] and water [17] nuclei, the temperature dependence of counterion and water splittings should differ markedly if either QCC varies strongly with temperature. As seen from Fig. 5, this is not the case; the splittings from the three nuclei have essentially the same temperature dependence and should therefore mainly reflect changes in ρ and/or S rather than in $\bar{\chi}$. The ratio of the water splittings is nearly constant, $v_Q(^{17}O)/v_Q(^2H) = 6.2 \pm 0.1$, as found in most systems and explained by the near degeneracy of the electric field gradient tensors of the ^{2}H and ^{17}O nuclei [17].
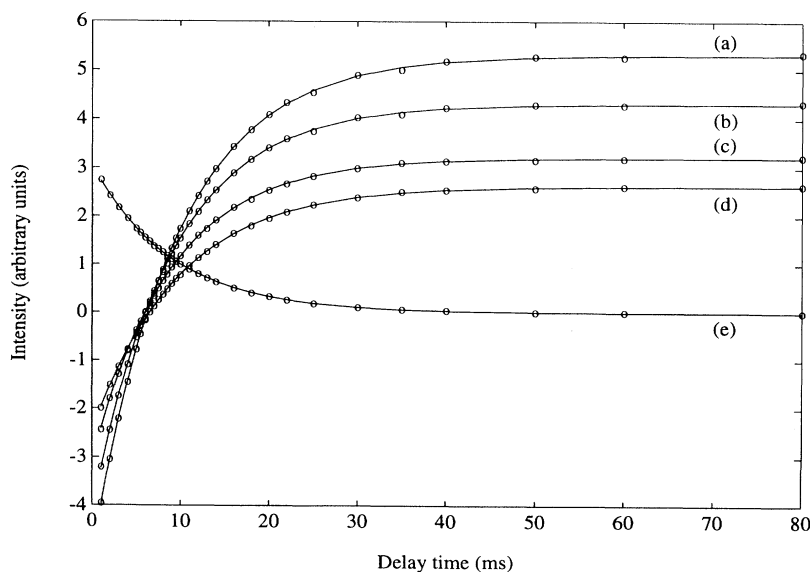

FIG. 3. The decay of the satellite (a) and central (b) lines in the inversion recovery experiment, the decay of the satellite (c) and central (d) lines in the inversion recovery experiment with short ($\sim 35°$) detection pulse, and the decay of the satellite lines (e) in the quadrupole polarization experiment at 2.0 T. The solid line resulted from a simultaneous fit to all experimental points (see text). The approximate error of a single point is ±0.03.
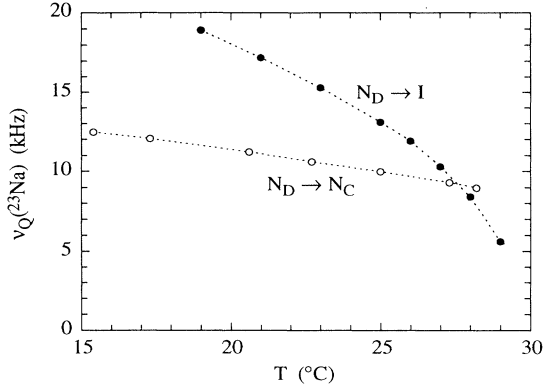
FIG. 4. Counterion ^{23}Na quadrupole splitting vs temperature in the N_D phase at two different compositions, transforming into an isotropic solution phase (this work) or into a calamitic nematic (N_C) phase [6]. The transition temperatures are $T_{N_D I}=29.3\,°C$ and $T_{N_D N_C}=28.8\,°C$.

IV. SPIN RELAXATION IN THE NEMATIC PHASE

A. Spectral density functions

The lab-frame spectral densities $J_1^L(\omega_0)$ and $J_2^L(2\omega_0)$ in Table III, derived from the ^{23}Na spin relaxation as described in Sec. II C, are cosine transforms of the time autocorrelation functions of the kth spherical component in the lab-fixed frame of the irreducible electric field gradient tensor at the nuclear position [7,18]. For a diamagnetically negative unixial nematic phase, these lab-frame spectral densities can be related, in a model-independent way, to three director-frame spectral density functions $J_m^D(\omega)$, with the symmetry axis of the nematic phase (i.e., the mean director) as the reference axis [6,19],

$$J_1^L(\omega_0)=\tfrac{1}{2}J_1^D(\omega_0)+\tfrac{1}{2}J_2^D(\omega_0) \ , \tag{4.1a}$$

$$J_2^L(2\omega_0)=\tfrac{3}{8}J_0^D(2\omega_0)+\tfrac{1}{2}J_1^D(2\omega_0)+\tfrac{1}{8}J_2^D(2\omega_0) \ . \tag{4.1b}$$
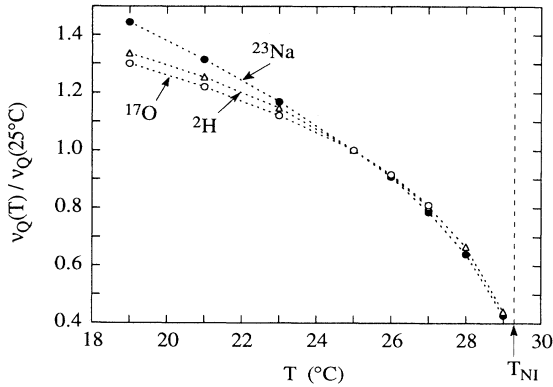

FIG. 5. Counterion ^{23}Na and water ^{2}H and ^{17}O quadrupole splittings, normalized relative to 25 °C, vs temperature in the N_D phase.

In principle, the biaxiality induced in the nematic phase by the external field (which is perpendicular to the principal symmetry axis of the phase) alters the form of the relations (4.1) [20]. At the relatively high Larmor frequencies ω_0 of interest here, however, this effect is negligible.

Under the conditions prevailing in an amphiphilic nematic phase, the director-frame spectral densities can be expressed as [6,21]

$$J_m^D(\omega)=J_{\text{loc}}+(\pi\bar\chi)^2 j_m^D(\omega;\rho,S) \ . \tag{4.2}$$

J_{loc} is the frequency-independent contribution from fast, weakly anisotropic, local (compared to micellar dimensions) motions [21]. The dependence on the desired parameters ρ and S enters via the reduced spectral densities $j_m^D(\omega)$, which reflect counterion surface diffusion on micelles of axial ratio ρ as well as restricted rotational diffusion of the entire micelle in the nematic potential of mean torque, (partly) characterized by the order parameter S. Since the surface diffusion of the Na$^+$ counterions is much faster than the restricted rotational diffusion of the relatively large micelle (cf. below), the reduced spectral density functions can be decomposed in two parts associated with rotation and surface diffusion, respectively [6,7],

$$j_m^D(\omega;\rho,S)=[A(\rho)]^2 H_{m0}^{\text{rot}}(S)\bar j_m^{\text{rot}}(\omega;\rho,S)$$

$$+\sum_{n=0}^{2}(2-\delta_{n0})[H_{mn}^{\text{rot}}(S)+\delta_{m0}\delta_{n0}S^2]$$

$$\times H_{n0}^{\text{sd}}(\rho)\bar j_n^{\text{sd}}(\omega;\rho) \ . \tag{4.3}$$

Here, we have explicitly displayed the initial values of the reduced time correlation functions,

$$H_{mn}^{\text{rot}}(S)=\langle[d_{mn}^2(\theta_{DA})]^2\rangle-\delta_{m0}\delta_{n0}S^2 \ , \tag{4.4a}$$

$$H_{n0}^{\text{sd}}(\rho)=\langle[d_{n0}^2(\theta_{AN})]^2\rangle-\delta_{n0}[A(\rho)]^2 \ , \tag{4.4b}$$

with θ_{DA} the angle between the symmetry axes of the nematic phase and the micellar aggregate, and θ_{AN} the angle between the micellar axis and the local normal to the micelle surface.

We model micelle reorientation in the N_D phase as rotational diffusion of a symmetric top in a potential of mean torque of the form $w(\theta_{DA})=-\lambda\cos^2\theta_{DA}$. This functional form, which can be regarded as the leading term in a multipole expansion consistent with the inversion symmetry of the micelle and the nematic phase, defines a unique relation between the second-rank and fourth-rank nematic order parameters and, hence, determines $H_{mn}^{\text{rot}}(S)$ in (4.4a) as a function of S. The reduced spectral densities $\bar j_m^{\text{rot}}(\omega)$ and $\bar j_n^{\text{sd}}(\omega)$ in (4.3), with the initial values of the corresponding time correlation functions factored out, can generally be expressed as linear combinations of Lorentzians,

$$\tilde j(\omega)=\sum_k c_k\frac{\tau_k}{1+(\omega\tau_k)^2} \ , \quad \sum_k c_k=1 \ . \tag{4.5}$$

The rotational spectral densities $\bar j_m^{\text{rot}}(\omega)$ in (4.3) involve only the rotational diffusion coefficient $D_\perp(\rho)$ determining the rate of tumbling of the micelle symmetry axis with respect to the nematic director. Under our condi-

tions, the $\bar{j}_m^{\mathrm{rot}}(\omega)$ are well approximated by a single Lorentzian term [7,22,23].

The three reduced surface-diffusion spectral density functions $\bar{j}_n^{\mathrm{sd}}(\omega)$ are completely determined by the micellar axial ratio ρ and a diffusional time constant which we define as $\tau_{\mathrm{sd}} = b^2/(4D_S)$, with D_S the Na$^+$ surface-diffusion coefficient and b a length comparable to the fully extended SDS molecule. The spectral density functions $\bar{j}_n^{\mathrm{sd}}(\omega)$ are usually not well approximated by single Lorentzians and we evaluate them numerically assuming an oblate spheroidal micelle shape [7]. For the relatively large axial ratios of interest here (cf. below), however, the energetics of local alkyl chain packing should favor a hemitoroidal disk over an oblate spheroid [24]. Since the surface-diffusion problem has not been solved for a hemitoroidal disk, we adapt (4.3) to the disk geometry by calculating $A(\rho)$ and $H_{n0}^{\mathrm{sd}}(\rho)$ exactly for a disk, while calculating $\bar{j}_n^{\mathrm{sd}}(\omega)$ for an oblate spheroid of the same axial ratio. This should be an acceptable approximation since the factors $A(\rho)$ and $H_{n0}^{\mathrm{sd}}(\rho)$ carry most of the ρ dependence and since, at the higher magnetic field that are most important in determining ρ, τ_{sd} is of order $1/\omega_0$ so that $\bar{j}_n^{\mathrm{sd}}(\omega)$ is relatively insensitive to τ_{sd}. The explicit expressions for $A(\rho)$ and $H_{n0}^{\mathrm{sd}}(\rho)$ for the disk geometry are given in the Appendix.

B. Quantitative data analysis

Before proceeding to a quantitative analysis of the relaxation and splitting data, we shall make a qualitative observation. As argued in Sec. III, the strong temperature dependence of the quadrupole splitting ν_Q (more than a factor 3 over 10 °C) is due to variations of ρ and/or S, rather than of the residual QCC $\bar{\chi}$. It is instructive to calculate the relative variation of the splitting and the lab-frame spectral densities for the two extreme cases of varying ρ at fixed S and varying S at fixed ρ. Figure 6 shows the results of such calculations at a relatively high magnetic field, where the contribution from micelle rotational dynamics is negligible. If the more than threefold decrease of ν_Q with T were due solely to a decrease of ρ, $J_1^L(\omega_0)$ would increase strongly with T (and, possibly, go through a maximum at high T). If, on the other hand, the decrease of ν_Q were due solely to a reduction of S with T, the surface-diffusion contribution to $J_1^L(\omega_0)$ would exhibit only a weak increase with T, which would be essentially canceled by the opposite T dependence of J_{loc} (cf. below). The observed near constancy of $J_1^L(\omega_0)$ in the investigated temperature interval at the higher fields (cf. Table III) clearly indicates that the second limiting case (varying S, constant ρ) is close to reality.

The analysis of the lab-frame spectral densities $J_1^L(\omega_0)$ and $J_2^L(2\omega_0)$ was performed within the model defined by (4.1)–(4.4), assuming a hemitoroidal disk shape for the micelles. Eliminating S by means of (3.1) and the measured splitting, we then have four parameters at each temperature: ρ, $\bar{\chi}$, J_{loc}, and τ_{sd}. [The tumbling diffusion coefficient $D_\perp(\rho)$ was calculated form the Perrin equations, using the experimental solvent viscosity.] The latter three parameters are determined by local interactions as the micelle interface and should not vary strongly
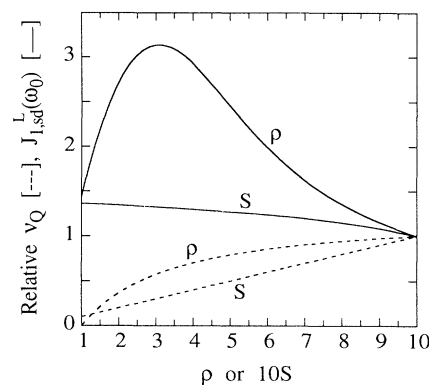

FIG. 6. Calculated relative variation of the quadrupole splitting (dashed) and the surface-diffusion contribution to the lab-frame spectral density $J_1^L(\omega_0)$ (solid) with the micellar axial ratio ρ at fixed $S = 0.75$ (curves labeled ρ), or with the nematic order parameter S at fixed $\rho = 5$ (curves labeled S). For the spectral density calculations, we used $B_0 = 1$ T and $\tau_{\mathrm{sd}} = 1.55$ ns.

between different liquid-crystalline phases as long as the aggregate composition (the SDS:decanol ratio) is roughly the same. We assume that the temperature dependence of these parameters is the same for the N_D phase as previously determined for the H_α phase [8], i.e., we write

$$\bar{\chi}(N_D, T) = c_\chi \bar{\chi}(H_\alpha, T) , \qquad (4.6a)$$

$$J_{\mathrm{loc}}(N_D, T) = c_J J_{\mathrm{loc}}(H_\alpha, T) , \qquad (4.6b)$$

$$\tau_{\mathrm{sd}}(N_D, T) = c_\tau \tau_{\mathrm{sd}}(H_\alpha, T) . \qquad (4.6c)$$

Including only relaxation data from the range $B_0 \geq 0.5$ T, where the least accurately modeled micelle rotation contribution is small or negligible (cf. below), we thus have seven adjustable parameters (c_χ, c_J, c_τ, and ρ at four temperatures) and 36 data (J_1^L and J_2^L at four temperatures and at four or six fields).

To examine the robustness of the analysis we have performed a large number of fits, varying the number of data points and the number of adjustable parameters. The results of some of these fits are shown in Table IV. It is clear that the micellar axial ratio is well determined by the data: ρ is in the range 4–6 and decreases weakly with temperature. Figure 7 shows the result of fit E together with the experimental data. Fits C and D were of similar quality. In fits A and B the agreement was good at the three highest temperatures, while the calculated spectral densities were slightly below the measured ones at 19 °C. This may be the result of forcing the H_α temperature dependence on the N_D data. This interpretation is consistent with the splitting data in Fig. 5, suggesting a somewhat stronger temperature dependence of $\bar{\chi}(^{23}\mathrm{Na})$ below 25 °C. The finding that $\bar{\chi}$ is large (by ca. 35%) in the N_D phase than in the H_α phase (cf. Table IV) is in accord with the previous finding [9] that $\bar{\chi}$ increases by ca. 30% on going from H_α to L_α (cf. Table I). In both cases, the increase of $\bar{\chi}$ presumably reflects the enhanced counterion accumulation at the less curved (higher surface charge density) aggregate surface. The contribution

TABLE IV. Parameter values determined from fits to ^{23}Na relaxation data and splittings from the N_D phase.

Fit	Data included B_0 range (T)	T range (°C)	Axial ratio, ρ 19°C	25°C	28°C	29°C	c_J	c_χ	c_τ
A	0.5–2.35	19–29	6.0	5.6	5.5	5.5	1.26	1.38	[1][a]
B	0.5–2.35	19–29	6.0	5.4	5.2	5.2	1.23	1.38	0.81
C	0.5–2.35	25–29		5.1	5.0	5.0	1.22	1.35	0.79
D	1.0–2.35	25–29		4.9	4.8	4.8	1.20	1.35	0.68
E	0.5–2.35	separate[b]	6.3	5.3	4.6	4.4	1.20–1.24	1.20–1.49	0.52–1.05

[a]Parameter value frozen in the fit.
[b]Data from each temperature fitted separately.

J_{loc} from fast local electric field gradient fluctuations, mainly associated with subpicosecond dynamics in the hydration shell of Na$^+$, is ca. 20% larger in N_D than in H_α (cf. Table IV). The surface-diffusion correlation time $\tau_{\mathrm{sd}} = b^2/(4D_S)$ is found to be shorter in N_D than in H_α. This is as expected, since the smallest aggregate dimension is usually close to the all-trans length of the amphiphilic molecule in the cylindrical aggregates of the H_α

phase, but is somewhat smaller in phases (L_α, N_D) with less curved microstructures. Finally, we note that if we model the micelles as oblate spheroids rather than as hemitroidal disks, we obtain axial ratios in the same range but fits of inferior quality.

The individual contributions to J_1^L and J_2^L from local dynamics (J_{loc}), surface diffusion, and micelle rotation are shown in Fig. 8. The ability of the field-dependent re-
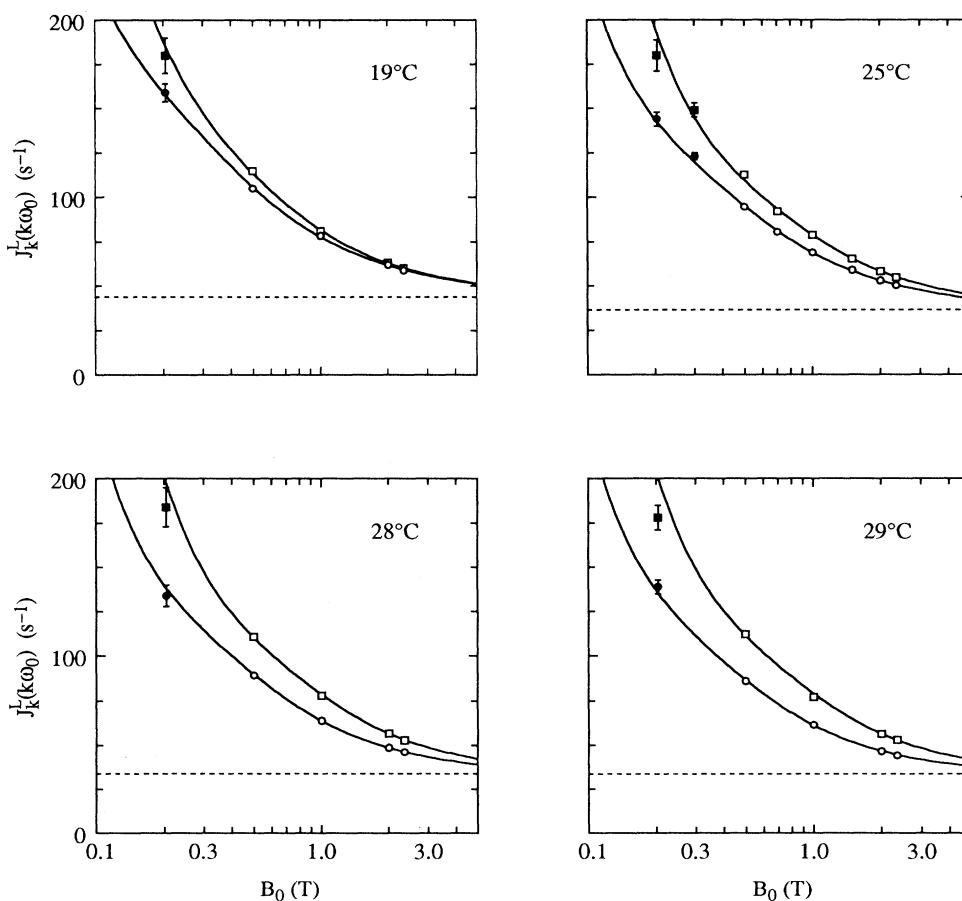

FIG. 7. Field dependence of the counterion ^{23}Na lab-frame spectral densities $J_1^L(\omega_0)$ (squares) and $J_2^L(2\omega_0)$ (circles) at four temperatures in the N_D phase. The curve resulted from least-squares fits (fit E in Table IV) to the data at $B_0 \geq 0.5$ T (open symbols) as described in the text. The dashed lines correspond to J_{loc}.
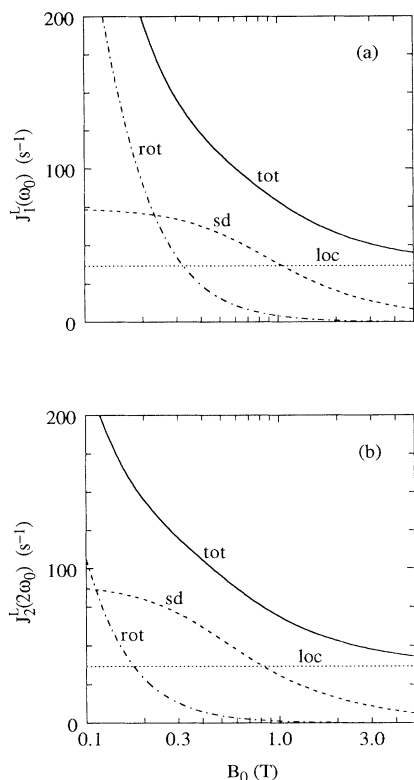
FIG. 8. Decomposition of the lab-frame spectral densities $J_1^L(\omega_0)$ and $J_2^L(2\omega_0)$ into their contributions from fast local motions (loc), counterion surface diffusion (sd), and micelle rotation (rot), calculated with the parameter values determined from the 25 °C fit in Fig. 7.

laxation data to accurately determine the micellar axial ratio is due to two facts, both apparent from Fig. 8. First, the investigated magnetic field range covers the major part of the surface-diffusion induced relaxation dispersion (which is sensitive to ρ—cf. Fig. 6). Second, the less accurately modeled rotational contribution is unimportant for $B_0 \geq 0.5$ T. As the field strength is decreased below this value, however, micelle rotation rapidly takes over as the dominant relaxation mechanism. At the lowest investigated field (0.2 T) micelle rotation contributes ca. 45% of $J_1^L(\omega_0)$ and ca. 20% of $J_2^L(2\omega_0)$. A deficiency in the rotational model should thus produce the largest discrepancy between theory and experiment for $J_1^L(\omega_0)$. This is indeed the case (cf. Fig. 7). The discrepancy is largest at the highest temperature, where the amplitude of the restricted micelle tumbling is largest (since S is relatively small) and, hence, the rotational model least accurate [22].

Using the parameters from the 25 °C fit, we have calculated the correlation times of the nine individual reorientational modes of a symmetric top in an even uniaxial potential of mean torque as well as the three effective surface-diffusion correlation times, defined as $\tau_n^{sd} = \tilde{j}_n^{sd}(0)$. (The latter are proportional to the parameter τ_{sd}, multiplied with a function of ρ that can only be obtained numerically [7].) These correlation times, as well as the ini-

tial values H_{mn}^{rot} and H_{n0}^{sd} of the corresponding time correlation functions, are shown in Table V. Since $\tau_n^{sd} \ll \tau_{mn}^{rot}$ for all modes, we were indeed justified in using the slow rotation approximation introduced in (4.3).

In the preceding, we tacitly assumed that the diffusive counterion exchange among the micelles is sufficiently slow not to affect the spectral densities $\tilde{j}_n^{sd}(\omega)$ and $\tilde{j}_m^{rot}(\omega)$. Since the diameter of the disklike micelles (ca. 200 Å) is substantially larger than the average separation between the surfaces of adjacent micelles (ca. 50 Å), we can estimate the mean residence time, τ_{res}, of a counterion with a given micelle as the mean-first-passage time [25] for surface-to-surface diffusion in a lamellar phase with the same surface separation and surface charge density as in the present N_D phase. If the ion diffused freely, τ_{res} would be ca. 10 ns; however, the strong electric field present in the intermicellar region increases τ_{res} to ca. 100 ns. Since this is much longer than the effective correlation times τ_n^{sd} for surface diffusion (cf. Table V), $\tilde{j}_n^{sd}(\omega)$ should be virtually unaffected by counterion exchange. The dominant micelle tumbling mode, with a correlation time $\tau_{10}^{rot} = 227$ ns, might be affected by counterion exchange, but the expected strong orientational correlation of adjacent micelles tends to reduce this effect [6].

A more serious concern is the collective nature of the reorientational dynamics in a nematic phase, which must be recognized at sufficiently low frequencies. Adopting the usual curvature-elastic continuum description [1], we have calculated the lowest-order director fluctuation contributions [26,27] to J_1^L and J_2^L. For a reasonable value of the short-wavelength cutoff, we find that these director fluctuation contributions are comparable to the independent-micelle rotation contributions included in our description. To properly describe the reorientational dynamics, we would need a more general theory that reduces to individual-micelle tumbling at high frequencies and to elastic-continuum director fluctuations at low frequencies. Fortunately, these complications do not seem to affect the determination of the micellar axial ratio from relaxation data in the range $B_0 \geq 0.5$ T.

Having determined ρ and $\bar{\chi}$, we can now obtain the nematic order parameter S from the quadrupole splitting ν_Q by means of (3.1). (The splitting was measured at

TABLE V. Effective correlation times and initial time correlation functions for micelle rotation and surface diffusion. Calculated with parameter values from the fit E at 25 °C.

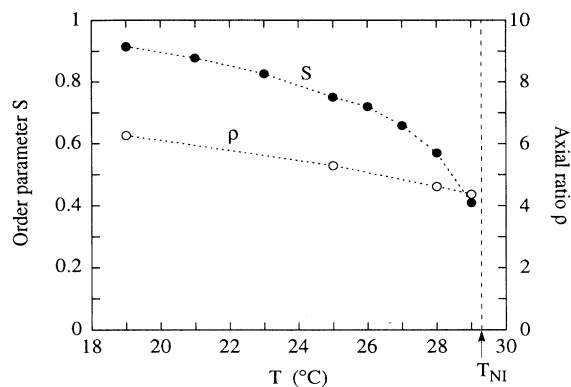| m	n	H_{mn}^{rot}	τ_{mn}^{rot} (ns)	n	H_{n0}^{sd}	τ_n^{sd} (ns)
0	0	0.063	184	0	0.278	4.6
0	1	0.165	230	1	0.086	5.6
0	2	0.021	150	2	0.068	9.5
1	0	0.165	227			
1	1	0.349	2591			
1	2	0.069	214			
2	0	0.021	145			
2	1	0.069	206			
2	2	0.421	778			

FIG. 9. Temperature dependence of the nematic order parameter S and the axial ratio ρ of the disk-shaped micelles in the N_D phase, derived from the ^{23}Na splitting and relaxation data of Figs. 4 and 7.

some additional temperatures in the range 19–29 °C; to calculate S at these temperatures, we use linearly interpolated values of ρ and $\bar{\chi}$.) Figure 9 shows the temperature variation of S (along with that of ρ) obtained in this way.

V. SPIN RELAXATION IN THE ISOTROPIC PHASE

To find out whether the micellar axial ratio changes at the N_D-I transition, we also measured the ^{23}Na spin relaxation dispersion in the isotropic phase at 30.5 °C, just above the transition. The measured effective longitudinal relaxation rate R_1^* is given by [13,28]

$$R_1^* = \tfrac{2}{5}[J_0^L(\omega_0) + 4J_0^L(2\omega_0)] . \tag{5.1}$$

Note that spin relaxation in an isotropic fluid involves only one lab-frame spectral density *function* and, thus, contains less information than the relaxation behavior in an anisotropic fluid, such as the nematic phase. In place of (4.2)–(4.4), we now have, in the slow-rotation limit [7],

$$J_0^L(\omega) = J_{\text{loc}} + \tfrac{1}{5}(\pi\bar{\chi})^2 \left\{ [A(\rho)]^2 \frac{\tau_\perp}{1+(\omega\tau_\perp)^2} \right.$$
$$\left. + \sum_{n=0}^{2} (2-\delta_{n0})H_{n0}^{\text{sd}}(\rho)\tilde{j}_n^{\text{sd}}(\omega) \right\} , \tag{5.2}$$

with $\tau_\perp = 1/(6D_\perp)$ the micelle tumbling correlation time in an isotropic medium.

The relaxation rate R_1^* is determined by the four parameters ρ, J_{loc}, $\bar{\chi}$, and τ_{sd} [with $D_\perp(\rho)$ calculated from the Perrin equations]. The later three parameters, being determined by local interactions, should have virtually the same values as in the N_D phase at the same temperature. We, thus, fixed these parameters to the values obtained by linearly extrapolating the N_D parameters from 29.0 to 30.5 °C. However, an acceptable fit of the R_1^* dispersion could not be obtained with the single adjustable parameter ρ. We, therefore, included the effect of

the finite counterion residence time, τ_{res}, on the micelle tumbling contribution through the replacement

$$\tau_\perp \rightarrow \frac{\tau_\perp \tau_{\text{res}}}{\tau_\perp + \tau_{\text{res}}} . \tag{5.3}$$

With the two adjustable parameters ρ and τ_{res} we obtained an excellent fit to the data in the range $B_0 \geq 0.5$ T. Again, as regards the determination of ρ, the fitting procedure appears to be robust (cf. Table VI). The result of fit *BI* is shown in Fig. 10; the other fits were of similar quality.

We, thus, find that the micellar axial ratio is increased to $\rho \approx 8$ just above the N_D-I transition. Since the result is contrary to theoretical predictions (cf. Sec. VI), a comment on its reliability is in order. The main cause for concern is whether the large axial ratio in the isotropic phase could be an artifact generated by an inaccurately modeled rotational contribution. As seen from Table VI, however, essentially the same axial ratio is obtained whether or not low-field data are included in the fit. In particular, virtually the same ρ value is obtained if we only include data from the range $B_0 \geq 1$ T, where the rotational contribution is negligible.

The counterion residence time τ_{res} is found to be ca. 100 ns, coinciding with our estimate of this quantity (cf. Sec IV B). (Since ρ is so large, adjacent micelles must be strongly correlated in the dense micellar solution. Consequently, the approximations used for this estimate should hold also for the isotropic phase.) It should be borne in mind, however, that this agreement might be fortuitous, since the parameter τ_{res} tends to compensate for deficiencies in our modeling of the micelle tumbling, which is expected to exhibit collective features at the lower frequencies. Since τ_{sd} is the least well determined parameter in the N_D dispersion fits, we investigated the effect of changing the fixed value of τ_{sd} from that obtained by extrapolating the N_D results to a value more in line with the results from the H_α phase [8]. While this had some effect on τ_{res}, ρ was virtually unaffected (cf. Table VI).

A comparison of Figs. 8 and 10 shows that the relative contribution from micelle tumbling is larger in the isotropic phase than in the N_D phase. It was, therefore, not necessary to take counterion exchange into account in the N_D fits. Inclusion of a fixed $\tau_{\text{res}} = 100$ ns in the N_D fits showed that, while τ_{res} and τ_{sd} are somewhat coupled (as in the isotropic fit), the other parameters were nearly unaffected (ρ decreased by less than 10%).

TABLE VI. Parameter values determined from fits to ^{23}Na relaxation data from the isotropic phase.

Fit	B_0 range (T)	ρ	τ_{res} (ns)	τ_{sd} (ns)
AI	1.0–2.35	8.3	97	[2.1][a]
BI	0.5–2.35	7.8	127	[2.1][a]
CI	0.2–2.35	7.6	145	[2.1][a]
DI	0.5–2.35	7.6	85	[1.5][a]

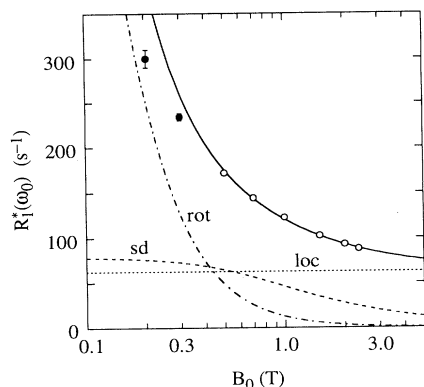[a]Parameter value frozen in the fit.

FIG. 10. Field dependence of the counterion ^{23}Na effective longitudinal relaxation rate R_1^* in the isotropic solution phase at 30.5 °C. The solid curve resulted from a least-squares fit to the data at $B_0 \geq 0.5$ T (open circles) as described in the text. The separate contributions to R_1^* from fast local motions (loc), counterion surface diffusion (sd), and micelle rotation (rot) were calculated with the parameter values determined from the fit.

VI. CONCLUDING DISCUSSION

The principal results of the present study may now be summarized.

(i) The combined relaxation and splitting data from the nematic and isotropic phases can be quantitatively accounted for by modeling the micelles as rigid hemitoroidal disks.

(ii) The axial ratio of the disklike micelles decreases slowly from 6 at 10 degrees below T_{NI} to 4 just below T_{NI}, but then abruptly increases to 8 at the N_D-I transition.

(iii) The nematic order parameter decreases from 0.9 at 10 °C below T_{NI} to 0.4 just below T_{NI}.

Our results for the micellar axial ratio in the nematic and isotropic phases may be compared with the results of a recent small-angle x-ray scattering study [29] of the isotropic phase in the same ternary system at 22 °C and similar water content; $n_W / (n_{SDS} + n_{dec}) = 40 - 44$ (cf. Table I). The axial ratio was reported to increase from 2 to 3 as the decanol content increased from $n_{dec} / (n_{SDS} + n_{dec}) = 0.03$ to 0.12. The micellar shape was reported to be spherocylindrical rather than disklike, which is reasonable since these samples have lower decanol content than ours (cf. Table I) and are close to the N_C phase (cf. Fig. 1). The progression from a more curved spherocylindrical to a less curved disklike micellar shape with increasing decanol content in the isotropic phase parallels the phase progression from N_C to N_D (cf. Fig. 1), and conforms with theoretical predictions of the effect of electrostatic interactions on micellar shape [30]. Our finding of a major change in micelle size at the N_D-I transition is in contrast to the insignificant change found at the same transition in a recent small-angle neutron scattering study of the system potassium laurate–decylammonium hydrochloride–water [31]. While large disklike micelles are not usually encountered in amphiphilic systems, their occurrence in the present isotropic phase sample is un-

derstandable in view of the nearby presence of the lamellar phase (cf. Fig. 1); our sample is isotropic at 30.5 °C but anisotropic (probably lamellar) at 33 °C.

The temperature variation of S is similar to what we have previously found for the N_C phase in the same system on approaching the N_C-I transition [6], but, as expected, differs markedly from the behavior of $S(T)$ in the same N_D phase (at a slightly higher micelle density) on approaching the N_D-N_C transition [6]. Although $S \approx 0.4$ at T_{NI} is close to the Maier-Saupe mean-field value $S(T_{NI}) = 0.43$, the temperature dependence of S is very much stronger than that predicted by the classical mean-field theory [1,32]. This discrepancy may be partly due to the substantial difference in micelle size on either side of the transition, with a consequent difference in the intermicellar interactions in the two phases. Another factor might be the importance of electrostatic interactions in ionic amphiphilic nematic phases. In any case, the present simultaneous determination of ρ and S across the nematic-isotropic transition should be of value for understanding the subtle interplay of orientational order, micelle size, and intermicellar and intramicellar interactions in amphiphilic nematic phases. To date this issue has been addressed theoretically only by rather crude hard-rod [33–36] or hard-disk [35] models, without explicit reference to electrostatic interactions. In contrast to our finding of a significant *increase* of ρ on going from the nematic to the isotropic phase, the existing theories predict a small [33,35] or a large [34,36] *decrease*. Furthermore, the theories predict a much higher degree of orientational order, typically $S(T_{NI}) \approx 0.8$, than found here and elsewhere [6,37]. Clearly, much remains to be done.

APPENDIX: INITIAL TIME CORRELATION FUNCTIONS FOR SURFACE DIFFUSION ON A HEMITOROIDAL DISK

Here, we give the explicit expressions for the quantities $H_{n0}^{sd}(\rho)$, defined by (4.4a), and the shape factor $A(\rho) = \langle P_2(\cos\theta_{AN}) \rangle$. The hemitoroidal disk consists of a flat (lamellar) part of radius R and thickness $2a$, surrounded by a curved edge of hemitoroidal shape. The axial ratio is defined as $\rho = (R + a)/a$.

By calculating the appropriate averages over the surface of the hemitoroidal disk, we obtain

$$H_{00}^{sd} = (64 + 55\pi\eta + 160\eta^2)/(160B) - A^2 , \qquad (A1a)$$

$$H_{10}^{sd} = (32 + 15\pi\eta)/(80B) , \qquad (A1b)$$

$$H_{20}^{sd} = (128 + 45\pi\eta)/(320B) , \qquad (A1c)$$

and

$$A = (\pi\eta + 4\eta^2)/(4B) , \qquad \text{(A2)}$$

with

$$B = 2 + \pi\eta + \eta^2 , \qquad \text{(A3)}$$

$$\eta = \rho - 1 . \qquad \text{(A4)}$$

The result (A2) has been given previously on two oc-

casions [3,38], albeit with typographical errors in both cases. We note that the present results have the correct limiting behavior. In the limit $\rho = 1$, when the hemitoroidal disk degenerates into a sphere, our results reduce to $H_{00}^{sd} = H_{10}^{sd} = H_{20}^{sd} = \frac{1}{5}$ and $A = 0$. In the limit $\rho \to \infty$, corresponding to an infinite lamella, we obtain $H_{00}^{sd} = H_{10}^{sd} = H_{20}^{sd} = 0$ and $A = 1$.

[1] P. G. de Gennes and J. Prost, *The Physics of Liquid Crystals*, 2nd ed. (Clarendon, Oxford, 1993).

[2] B. J. Forrest and L. W. Reeves, Chem. Rev. **81**, 1 (1981).

[3] J. Charvolin and Y. Hendrikx, in *Nuclear Magnetic Resonance of Liquid Crystals*, edited by J. W. Emsley (Reidel, Dordrecht, 1985), p. 449.

[4] A. S. Sonin, Usp. Fiz. Nauk. **153**, 273 (1987) [Sov. Phys. Usp. **30**, 875 (1987)].

[5] N. Boden, P. J. B. Edwards, and K. W. Jolley, in *Structure and Dynamics of Strongly Interacting Colloids and Supramolecular Aggregates in Solution*, edited by S.-H. Chen, J. S. Huang, and P. Tartaglia (Kluwer, Dordrecht, 1992), p. 433.

[6] P-O. Quist, B. Halle, and I. Furó, J. Chem. Phys. **96**, 3875 (1992).

[7] B. Halle, J. Chem. Phys. **94**, 3150 (1991).

[8] P-O. Quist, B. Halle, and I. Furó, J. Chem. Phys. **95**, 6945 (1991).

[9] P-O. Quist and B. Halle, Phys. Rev. E **47**, 3374 (1993).

[10] J. Jeener and P. Broekaert, Phys. Rev. **157**, 232 (1967).

[11] I. Furó and B. Halle, J. Chem. Phys. **91**, 42 (1989).

[12] A. D. Bain, J. Magn. Reson. **89**, 153 (1990).

[13] P. S. Hubbard, J. Chem. Phys. **53**, 985 (1970).

[14] P. Huang Kenéz, G. Carlström, I. Furó, and B. Halle, J. Phys. Chem. **96**, 9524 (1992).

[15] G. Jaccard, S. Wimperis, and G. Bodenhausen, J. Chem. Phys. **85**, 6282 (1986).

[16] P. Linse and B. Halle, Mol. Phys. **67**, 537 (1989).

[17] B. Halle and H. Wennerström, J. Chem. Phys. **75**, 1928 (1981).

[18] A. Abragam, *The Principles of Magnetic Resonance* (Clarendon, Oxford, 1961).

[19] S. Gustafsson and B. Halle, Mol. Phys. **80**, 549 (1993).

[20] B. Halle, Liq. Cryst. (to be published).

[21] B. Halle, P-O. Quist, and I. Furó, Liq. Cryst. **14**, 227 (1993).

[22] G. Moro and P. L. Nordio, Chem. Phys. Lett. **96**, 192 (1983).

[23] A. Szabo, J. Chem. Phys. **81**, 150 (1984).

[24] J. N. Israelachvivli, D. J. Mitchell, and B. W. Ninham, J. Chem. Soc. Faraday Trans. 2 **72**, 1525 (1976).

[25] D. Y. C. Chan and B. Halle, Biophys. J. **46**, 387 (1984).

[26] P. Pincus, Solid State Commun. **7**, 415 (1969).

[27] R. Y. Dong, *Nuclear Magnetic Resonance of Liquid Crystals* (Springer-Verlag, New York, 1994).

[28] B. Halle and H. Wennerström, J. Magn. Reson. **44**, 89 (1981).

[29] R. Itri and L. Q. Amaral, Phys. Rev. E **47**, 2551 (1993).

[30] B. Halle, M. Landgren, and B. Jönsson, J. Phys. (Paris) **49**, 1235 (1988).

[31] V. Formoso, Y. Galerne, F. P. Nicoletta, G. Pepy, N. Picci, and R. Bartolino, J. Phys. (Paris) Colloq. **3**, C1 (1993); **3**, C271 (1993).

[32] W. Maier and A. Saupe, Z. Naturforsch. Teil A **13**, 564 (1958); **14**, 882 (1959); **15**, 287 (1960).

[33] W. M. Gelbart, W. E. McMullen, and A. Ben-Shaul, J. Phys. (Paris) **46**, 1137 (1985).

[34] T. Odijk, J. Phys. (Paris) **48**, 125 (1987).

[35] M. P. Taylor and J. Herzfeld, Phys. Rev. A **43**, 1892 (1991).

[36] P. van der Schoot and M. E. Cates, Langmuir **10**, 670 (1994).

[37] N. Boden, S. A. Corne, M. C. Holmes, P. H. Jackson, D. Parker, and K. W. Jolley, J. Phys. (Paris) **47**, 2135 (1986).

[38] M. R. Kuzma, J. Phys. Chem. **89**, 4124 (1985).